

Active Orbital Debris Removal Using Space Robotics

Farhad Aghili

Canadian Space Agency

St-Hubert, QC, Canada, email: farhad.aghili@asc-csa.gc.ca

Abstract

One of the main technical challenge in orbital debris removal (ODR) missions is how to capture a tumbling and drifting space object given several environmental and operational constraints. This paper focuses on the guidance of a robot manipulator in a pre- and post-grasp phases to capture and stabilize a drifting and tumbling space object with uncertain dynamics. A Kalman filter is used to estimate the states and dynamics parameters of target based on data received from a vision system. In the pre-grasping phase, a time-optimal trajectory is planned to intercept a grasping point on the target with zero relative velocity subject to acceleration limit and adequate target alignment. In the post-grasping phase, the manipulator damps out the initial angular and linear momentums as quickly as possible subject to maximum exerted force and torque. Experiments are presented to demonstrate the robot-motion planning scheme for autonomous grasping of a tumbling satellite.

1 Introduction

Orbital debris is defined as the collection of man-made objects in space whose size may range from small pieces released during satellite deployment to massive defunct satellites and rocket bodies. Despite all orbital debris eventually reenter the Earth atmosphere within few years or centuries, depending on their size and orbit, space debris is on the rise owing to the increasing rate of satellite launches and retirements [1]. Nowadays the international concern is that the population growth has reached an unstable point in some congested orbits such that the collision between orbital debris objects could cause a cascade scenario—the Kessler syndrome [2]. Based on Inter Agency Debris Coordination (IADC) recommendations, the space environment can be stabilized and preserved upon continual removal of large orbital debris objects. A comprehensive concept for active orbital debris removal (ODR) system makes use of a servicing spacecraft equipped with a robotic

system with grappling device on it [3,4]. After being launched, such ODR system must provide the following functional capabilities: i) orbital maneuvering, e.g., orbit-to-orbit transfer and rendezvous with a selected debris; ii) rendezvous with the selected orbital debris; iii) capturing the orbital object and dissipating its angular momentum; iv) transferring the captured orbital object to either a “graveyard orbit” or to a low orbit for reentering to Earth’s atmosphere within maximum 25 years.

Since orbital debris objects do not have a functional attitude control system, it is common for them to tumble. Ground observations also reveal that many space debris objects do have tumbling motion indeed [5]. Experiments conducted on ISS revealed that, in the presence of command latency, even a trained operator cannot successfully capture a free-floater unless the angular rate is extremely low. In fact, although several missions for free-flyer capture using a robotic arm on-orbit have been demonstrated so far [6–9], robotic capturing of a tumbling satellite has not been attempted yet. As such, increased autonomy for robotic systems for on-orbit servicing missions is identified as the key technology by many space agencies [10].

This work presents pre-grasping and post-grasping motion planning schemes for autonomous robotic capture of a tumbling space object using vision feedback. First, an adaptive Kalman filter gives estimations of the motion states and the dynamics parameters of the free-floating target from noisy measurements of a laser camera system. This allows the motion of the target to be reliably predicted as soon as the filter converges. Subsequently, the estimated states are used to plan the trajectory of the robot’s end-effector in the pre-grasping and post-grasping phases. In the pre-grasping phase, the robot motion to intercept the object in minimum time is planned subject to robot acceleration limit and the following constraints at the time of interception: i) the robot’s end-effector and the target’s grapple fixture have zero relative velocity therefore the capture is with minimum impact; ii) the target object is adequately aligned with respect to the robot such the fixture on

the target becomes accessible for robotic grasping. In the post-grasping phase, when the end-effector mechanically connects to the target, the manipulator stabilizes the drifting and tumbling target satellite as quickly as possible without applying excessive force and torque. This paper is organized as follow: Section 2 describes the design of a Kalman estimator for state/parameter estimation and motion prediction of the target, planning optimal trajectories in the pre- and pos-grasping phases are, respectively, described in Sections 3 and 4. Finally experimental results obtained from a hardware-in-the-loop simulation are presented in Section 5.

2 Target Motion and Parameters Estimation

The implementation of optimal motion-planning trajectories, which will be later described in the next sections, requires the values of the full motion states as well as the dynamic parameters of the target. Since the vision system gives only measurement of the object pose, we need to estimate the rest of variables. This section describes an extended EKF-based estimator to estimate not only the system states but also all the relevant parameters.

Fig. 1 illustrates a robot trying to capture a drifting and tumbling object. $\{A\}$ is assumed the inertial frame, while coordinate frame $\{B\}$ is attached to the body of the target. Coordinate frame $\{C\}$ is fixed to the target's grapple fixture located at $\boldsymbol{\rho}$ from the origin of $\{B\}$; it is the pose of $\{C\}$ which is measured by the vision system. We further assume that the target tumbles with angular velocity $\boldsymbol{\omega}$. Since it is not possible to identify the absolute values of the inertia parameters from observations of torque-free tumbling motion [11], we use the following non-dimensional inertia parameters

$$p_x = \frac{I_{yy} - I_{zz}}{I_{xx}}, \quad p_y = \frac{I_{zz} - I_{xx}}{I_{yy}}, \quad p_z = \frac{I_{xx} - I_{yy}}{I_{zz}} \quad (1)$$

where I_{xx} , I_{yy} , and I_{zz} denote the target's principal moments of inertia, and $\mathbf{I}_c = \text{diag}(I_{xx}, I_{yy}, I_{zz})$ is the corresponding inertia tensor. Then, the Euler's equations can be expressed in terms of relative inertia parameters $\mathbf{p} = [p_x \ p_y \ p_z]^T$ as

$$\dot{\boldsymbol{\omega}} = \mathbf{d}(\boldsymbol{\omega}, \mathbf{p}) + \mathbf{B}(\mathbf{p})\boldsymbol{\epsilon}_\tau \quad (2)$$

where

$$\mathbf{d}(\boldsymbol{\omega}, \mathbf{p}) = \begin{bmatrix} p_x \omega_y \omega_z \\ p_y \omega_x \omega_z \\ p_z \omega_x \omega_y \end{bmatrix}, \quad \mathbf{B} = \begin{bmatrix} b_x(\mathbf{p}) & 0 & 0 \\ 0 & b_y(\mathbf{p}) & 0 \\ 0 & 0 & b_z(\mathbf{p}) \end{bmatrix},$$

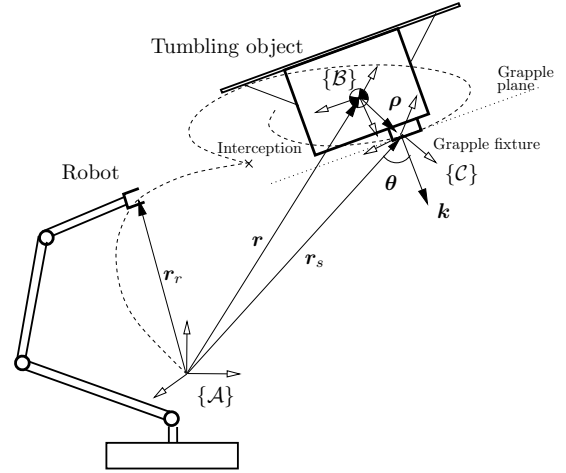


Figure 1: Robotic capturing of a free-floating tumbling object.

$$\begin{aligned} b_x(\mathbf{p}) &= 1 + \frac{1 + p_x}{1 - p_y} + \frac{1 - p_x}{1 + p_z} \\ b_y(\mathbf{p}) &= 1 + \frac{1 + p_y}{1 - p_z} + \frac{1 - p_y}{1 + p_x} \\ b_z(\mathbf{p}) &= 1 + \frac{1 + p_z}{1 - p_x} + \frac{1 - p_z}{1 + p_y} \end{aligned} \quad (3)$$

and $\boldsymbol{\epsilon}_\tau = \boldsymbol{\tau}/\text{tr}(\mathbf{I}_c)$ is defined as the acceleration disturbance with $\text{tr}(\cdot)$ denoting the trace of a matrix. Here, the process noise is assumed to be with covariance $E[\boldsymbol{\epsilon}_\tau \boldsymbol{\epsilon}_\tau^T] = \sigma_\tau^2 \mathbf{1}_3$.

Let quaternion $\mathbf{q} = [\mathbf{q}_v^T \ q_o]^T$ represent the orientation of the target. Then, the time derivative of the quaternion can be expressed by

$$\dot{\mathbf{q}} = \frac{1}{2} \boldsymbol{\Omega}(\boldsymbol{\omega}) \mathbf{q} \quad \text{where} \quad \boldsymbol{\Omega}(\boldsymbol{\omega}) = \begin{bmatrix} -[\boldsymbol{\omega} \times] & \boldsymbol{\omega} \\ -\boldsymbol{\omega}^T & 0 \end{bmatrix} \quad (4)$$

Coincidentally, the matrix function $\boldsymbol{\Omega}(\cdot)$ also appears in the quaternion product. Let us define operator \otimes acting on quaternion \mathbf{q} as

$$\mathbf{q} \otimes \triangleq q_o \mathbf{1}_4 + \boldsymbol{\Omega}(\mathbf{q}_v) \quad (5)$$

The translational motion of the target can be simply expressed by

$$\ddot{\mathbf{r}} = \boldsymbol{\epsilon}_f \quad (6)$$

where \mathbf{r} denotes the location of the target CM expressed in the inertial frame $\{A\}$, and $\boldsymbol{\epsilon}_f$ is the disturbance force per unit mass, which is assumed to be white noise with covariance $E[\boldsymbol{\epsilon}_f \boldsymbol{\epsilon}_f^T] = \sigma_f^2 \mathbf{1}_3$. Consider the state vector to be estimated by KF as

$$\mathbf{x} = [\mathbf{q}_v^T \ \boldsymbol{\omega}^T \ \mathbf{r}^T \ \dot{\mathbf{r}}^T \ \mathbf{p}^T \ \boldsymbol{\rho}^T \ \boldsymbol{\mu}_v^T]^T \quad (7)$$

where ρ is the location of target's center of mass and η is a unit quaternion representing the orientation of the principal axes, i.e., orientation of $\{\mathcal{B}\}$ w.r.t. $\{\mathcal{C}\}$. Now, assume that the dynamics parameters of the target \mathbf{p} , ρ , and η remain constant, the process dynamics including (2), (4), and (6) can be described in this compact form

$$\dot{\mathbf{x}} = \mathbf{f}_s(\mathbf{x}) + \mathbf{G}(\mathbf{x})\epsilon, \quad (8)$$

where

$$\mathbf{G}(\mathbf{x}) = \begin{bmatrix} \mathbf{0}_3 & \mathbf{0}_3 \\ \mathbf{B}(\mathbf{p}) & \mathbf{0}_3 \\ \mathbf{0}_3 & \mathbf{0}_3 \\ \mathbf{0}_3 & \mathbf{1}_3 \\ \mathbf{0}_{9 \times 3} & \mathbf{0}_{9 \times 3} \end{bmatrix} \quad \text{and} \quad \epsilon = \begin{bmatrix} \epsilon_\tau \\ \epsilon_f \end{bmatrix}$$

Linearization of vector \mathbf{f}_s in (8) needed to be used for covariance propagation of extended Kalman filter can derived as

$$\mathbf{F} = \frac{\partial \mathbf{f}_s(\mathbf{x})}{\partial \mathbf{x}} \Big|_{\mathbf{x}=\hat{\mathbf{x}}} \quad (9)$$

$$= \begin{bmatrix} -[\hat{\omega} \times] & \frac{1}{2}\mathbf{1}_3 & \mathbf{0}_3 & \mathbf{0}_3 & \mathbf{0}_3 & \mathbf{0}_3 & \mathbf{0}_{3 \times 6} \\ \mathbf{0}_3 & \mathbf{M}(\hat{\omega}, \hat{\mathbf{p}}) & \mathbf{0}_3 & \mathbf{0}_3 & \mathbf{0}_3 & \mathbf{N}(\hat{\omega}) & \mathbf{0}_{3 \times 6} \\ \mathbf{0}_3 & \mathbf{0}_3 & \mathbf{0}_3 & \mathbf{1}_3 & \mathbf{0}_3 & \mathbf{0}_3 & \mathbf{0}_{3 \times 6} \\ \mathbf{0}_{12 \times 3} & \mathbf{0}_{12 \times 3} & \mathbf{0}_{12 \times 3} & \mathbf{0}_{12 \times 3} & \mathbf{0}_{12 \times 3} & \mathbf{0}_{12 \times 3} & \mathbf{0}_{12 \times 6} \end{bmatrix},$$

where

$$\mathbf{M} = \begin{bmatrix} 0 & \hat{p}_x \hat{\omega}_z & \hat{p}_x \hat{\omega}_y \\ \hat{p}_y \hat{\omega}_z & 0 & \hat{p}_y \hat{\omega}_x \\ \hat{p}_z \hat{\omega}_y & \hat{p}_z \hat{\omega}_x & 0 \end{bmatrix}, \quad \mathbf{N} = \begin{bmatrix} \hat{\omega}_y \hat{\omega}_z & 0 & 0 \\ 0 & \hat{\omega}_x \hat{\omega}_z & 0 \\ 0 & 0 & \hat{\omega}_x \hat{\omega}_y \end{bmatrix}.$$

Suppose that the vision system gives a noisy measurement of the position and orientation of coordinate $\{\mathcal{C}\}$ attached to the grapple fixture with respect to the inertial coordinate system $\{\mathcal{A}\}$; see Fig. 1. Denoting the orientation of $\{\mathcal{C}\}$ with respect to $\{\mathcal{A}\}$ by unit quaternion η , one can write the measurement vector as

$$\mathbf{z} = \begin{bmatrix} \mathbf{r}_s \\ \eta \end{bmatrix} + \mathbf{v} \quad (10)$$

where the position and orientation are represented by vector \mathbf{r}_s and unit quaternion η , and \mathbf{v} is the measurement noise with covariance $\mathbf{R} = E[\mathbf{v}\mathbf{v}^T]$. The orientation of the principal axes is not a priori known and so is not the alignment of coordinate frame $\{\mathcal{C}\}$ with respect to $\{\mathcal{B}\}$. The quaternion η can be considered as two successive orientations as

$$\eta = \boldsymbol{\mu} \otimes \mathbf{q}. \quad (11)$$

where $\boldsymbol{\mu}$ represents the orientation of the principal axes. Then, the observation equations can be written as a nonlinear function of the states

$$\mathbf{z} = \mathbf{h}(\mathbf{x}) + \mathbf{v} \quad \text{where} \quad \mathbf{h}(\mathbf{x}) = \begin{bmatrix} \mathbf{r} + \mathbf{A}(\mathbf{q})\rho \\ \boldsymbol{\mu} \otimes \mathbf{q} \end{bmatrix} \quad (12)$$

where

$$\mathbf{A}(\mathbf{q}) = (2q_o^2 - 1)\mathbf{1}_3 + 2q_o[\mathbf{q}_v \times] + 2\mathbf{q}_v \mathbf{q}_v^T \quad (13)$$

is the corresponding rotation matrix. The observation sensitivity matrix can be obtained as

$$\mathbf{H} = \frac{\partial \mathbf{h}(\mathbf{x})}{\partial \mathbf{x}} \Big|_{\mathbf{x}=\hat{\mathbf{x}}} \quad (14)$$

$$= \begin{bmatrix} -2\mathbf{A}(\hat{\mathbf{q}})[\hat{\rho} \times] & \mathbf{0}_{3 \times 3} & \mathbf{1}_3 & \mathbf{0}_{3 \times 6} & \mathbf{A}(\hat{\mathbf{q}}) & \mathbf{0}_{3 \times 3} \\ \boldsymbol{\Upsilon}(\hat{\mathbf{q}}, \hat{\boldsymbol{\mu}}) & \mathbf{0}_{4 \times 3} & \mathbf{0}_{4 \times 3} & \mathbf{0}_{4 \times 6} & \mathbf{0}_{4 \times 3} & \boldsymbol{\Upsilon}(\hat{\mathbf{q}}, \hat{\boldsymbol{\mu}}) \end{bmatrix},$$

where

$$\boldsymbol{\Upsilon} = \begin{bmatrix} \hat{q}_o \hat{\eta}_o \mathbf{1}_3 - \hat{q}_o [\hat{\boldsymbol{\mu}}_v \times] + \hat{\eta}_o [\hat{\mathbf{q}}_v \times] - [\hat{\mathbf{q}}_v \times] [\hat{\boldsymbol{\mu}}_v \times] - \hat{\mathbf{q}}_v \hat{\boldsymbol{\mu}}_v^T \\ (\hat{\mathbf{q}}_v \times \hat{\boldsymbol{\mu}}_v)^T - \hat{\eta}_o \hat{\mathbf{q}}_v^T - \hat{q}_o \hat{\boldsymbol{\mu}}_v^T \end{bmatrix}.$$

Now, one can design an extended Kalman filter (EKF) based on the derived linearized models (9) and (14).

3 Pre-Grasping Trajectory Planning

The main objective in the pre-capturing phase is to bring the end-effector from its initial position $\mathbf{r}_r(t_o)$ at initial time $t = t_o$ to a grasping location along the trajectory of the grapple fixture on the target satellite while satisfying the acceleration magnitude constraint $\|\ddot{\mathbf{r}}_r(t)\| \leq a$ for $t \in [t_o, t_f]$ and terminal conditions

$$\mathbf{r}_r(t_f) = \mathbf{r}_s(t_f) \quad \text{and} \quad \dot{\mathbf{r}}_r(t_f) = \dot{\mathbf{r}}_s(t_f). \quad (15)$$

In order to gauge the accessibility of the grapple fixture by the robot, let us define the line of sight angle θ that is made by the opposite direction of vector \mathbf{r}_r (at the time of interception) and unit vector \mathbf{k} attached to the grapple fixture; see Fig. 1. It is assumed that vector \mathbf{k} is expressed in the target frame $\{\mathcal{C}\}$ in such a way that $\theta = 0$ corresponds to the most suitable object alignment for robotic grasping and conversely the grasping is not possible when $\theta = \pi$. Now, assume that the optimal trajectory is generated by the following second order system

$$\ddot{\mathbf{r}}_r = \mathbf{u}, \quad (16)$$

Now, denoting the state vector of the entire system as

$$\mathbf{x} = [\mathbf{q}^T \ \boldsymbol{\omega}^T \ \mathbf{r}^T \ \dot{\mathbf{r}}_r^T \ \dot{\mathbf{r}}_r^T]^T,$$

we get the following autonomous system

$$\dot{\mathbf{x}}(\mathbf{x}, \mathbf{u}) = \begin{bmatrix} \frac{1}{2}\boldsymbol{\Omega}(\boldsymbol{\omega})\mathbf{q} \\ \mathbf{d}(\boldsymbol{\omega}) \\ \dot{\mathbf{r}} \\ \dot{\mathbf{r}}_r \\ \mathbf{u} \end{bmatrix}, \quad (17)$$

because the drift velocity, $\dot{\mathbf{r}}$, is constant.

In the following analysis, an optimal solution to the input \mathbf{u} of system (17) is sought to minimize the following cost function

$$J = \phi[\mathbf{x}(t_f)] + \int_{t_o}^{t_f} 1 + c(\mathbf{u})d\tau, \quad (18)$$

where

$$c(\mathbf{u}) = \begin{cases} \kappa(\|\mathbf{u}\|^2 - a^2) & \text{if } \|\mathbf{u}\| \geq a \\ 0 & \text{otherwise} \end{cases} \quad (19)$$

is a penalty function, subject to the following terminal state constraint

$$\psi[\mathbf{x}(t_f)] = \mathbf{0}. \quad (20)$$

The terminal state constraint is

$$\psi(\mathbf{x}) = \begin{bmatrix} \mathbf{r}_s - \mathbf{r}_r \\ \dot{\mathbf{r}}_s - \dot{\mathbf{r}}_r \end{bmatrix}, \quad (21)$$

where

$$\mathbf{r}_s = \mathbf{r} + \mathbf{A}(\mathbf{q})\boldsymbol{\rho} \quad (22a)$$

$$\dot{\mathbf{r}}_s = \dot{\mathbf{r}} + \mathbf{A}(\mathbf{q})(\boldsymbol{\omega} \times \boldsymbol{\rho}). \quad (22b)$$

The non-integral part of the cost function (18) is set to

$$\phi(\mathbf{x}) = w_1 \|\mathbf{r}_r\| - w_2 \cos \theta, \quad (23)$$

where $w_1 > 0$ and $w_2 > 0$ are scalar weights. Clearly, the incorporation of ϕ in the cost function tends to minimize the distance $\|\mathbf{r}_r(t_f)\|$ and the line-of-sight angle $\theta(t_f)$. Denoting $\mathbf{k}'(\mathbf{q}) = \mathbf{A}(\mathbf{q})\mathbf{k}$, one can readily express the cosine as

$$\cos \theta = -\frac{\mathbf{r}_r \cdot \mathbf{k}'(\mathbf{q})}{\|\mathbf{r}_r\|}.$$

The Hamiltonian for system (17) and (18) can be written as

$$\mathcal{H} = 1 + c(\mathbf{u}) + \boldsymbol{\lambda}^T \dot{\mathbf{x}}(\mathbf{x}, \mathbf{u}) \quad (24)$$

According to the optimal control theory [12], the costate and optimal input, \mathbf{u}^* , must satisfy the following partial derivatives:

$$\dot{\boldsymbol{\lambda}} = -\frac{\partial \mathcal{H}}{\partial \mathbf{x}}, \quad \frac{\partial \mathcal{H}}{\partial \mathbf{u}} = \mathbf{0}. \quad (25)$$

Splitting the vector of costate as $\boldsymbol{\lambda} = [\boldsymbol{\lambda}_s^T \ \boldsymbol{\lambda}_r^T \ \boldsymbol{\lambda}_u^T]^T$, where $\boldsymbol{\lambda}_s \in \mathbb{R}^9$ and $\boldsymbol{\lambda}_r, \boldsymbol{\lambda}_u \in \mathbb{R}^3$, and the applying (25) to our Hamiltonian (24) yields the following identities

$$\dot{\boldsymbol{\lambda}}_r = \mathbf{0} \quad (26a)$$

$$\dot{\boldsymbol{\lambda}}_u = -\boldsymbol{\lambda}_r \quad (26b)$$

$$\boldsymbol{\lambda}_u = -2\kappa\mathbf{u}^* \quad (26c)$$

One can readily infer from (26a)–(26c) that the expression of the acceleration trajectory is:

$$\mathbf{u}^* = \boldsymbol{\alpha}(t - t_o) + \boldsymbol{\beta}, \quad (27)$$

where $\boldsymbol{\alpha}$ and $\boldsymbol{\beta}$ are defined such that

$$\begin{aligned} \boldsymbol{\lambda}_r &= 2\kappa\boldsymbol{\alpha} \\ \boldsymbol{\lambda}_u &= -2\kappa\boldsymbol{\alpha}(t - t_o) - 2\kappa\boldsymbol{\beta} \end{aligned} \quad (28)$$

Subsequently, one can obtain the position and velocity trajectories via integration. The constant polynomial coefficients $\boldsymbol{\alpha}$ and $\boldsymbol{\beta}$ are solved by imposing the initial and terminal conditions (21)

$$\begin{aligned} \boldsymbol{\alpha} &= \frac{6(\dot{\mathbf{r}}_s(t_f) + \dot{\mathbf{r}}_r(t_o))}{(t_f - t_o)^2} - \frac{12(\mathbf{r}_s(t_f) - \mathbf{r}_r(t_o))}{(t_f - t_o)^3} \\ \boldsymbol{\beta} &= -\frac{2(\dot{\mathbf{r}}_s(t_f) + 2\dot{\mathbf{r}}_r(t_o))}{t_f - t_o} + \frac{6(\mathbf{r}_s(t_f) - \mathbf{r}_r(t_o))}{(t_f - t_o)^2} \end{aligned} \quad (29)$$

The expression of the optimal control input in (27), (29) can be written as a function of initial time, t_o , and current time, t , in this form

$$\mathbf{u}^*(t_o, t) = \boldsymbol{\Gamma}(t_o, t)\mathbf{e}(t) + \boldsymbol{\gamma}(t_o, t) \quad t \in [t_o, t_f] \quad (30)$$

where

$$\mathbf{e}(t) = \begin{bmatrix} \mathbf{r}_s(t_f) - \mathbf{r}_r(t) \\ \dot{\mathbf{r}}_s(t_f) - \dot{\mathbf{r}}_r(t) \end{bmatrix}$$

can be treated as the feedback error on which a controller with following time-varying feedback gain acts

$$\begin{aligned} \boldsymbol{\Gamma}(t_o, t) &= \begin{bmatrix} \frac{-12t+6t_o+6t_f}{(t_f-t_o)^3}\mathbf{1}_3 & \frac{6t-4t_o-2t_f}{(t_f-t_o)^2}\mathbf{1}_3 \end{bmatrix} \\ \boldsymbol{\gamma}(t_o, t) &= \frac{12t-6t_o-6t_f}{(t_f-t_o)^2}\dot{\mathbf{r}}_s(t_f) \end{aligned} \quad (31)$$

Now, the control input at any given time $t \in [t_o, t_f]$ can be also calculated by setting the values of the position and velocity at that time as the initial values in (30). Therefore, by setting the floating initial time $t_o = t$ in (31), we will arrive at

$$\begin{aligned} \boldsymbol{\Gamma}(t, t) &= \begin{bmatrix} \frac{6}{(t_f-t)^2}\mathbf{1}_3 & \frac{-2}{t_f-t}\mathbf{1}_3 \end{bmatrix} \\ \boldsymbol{\gamma}(t, t) &= \frac{-6}{t_f-t}\dot{\mathbf{r}}_s(t_f) \end{aligned} \quad (32)$$

Finally, using shorthand notation $\mathbf{u}^*(t, t) = \mathbf{u}^*(t)$, $\boldsymbol{\Gamma}(t, t) = \boldsymbol{\Gamma}(t)$, and $\boldsymbol{\gamma}(t, t) = \boldsymbol{\gamma}(t)$, one can rewrite (30) as

$$\ddot{\mathbf{r}}_r^* = \begin{cases} \boldsymbol{\Gamma}(t)\mathbf{e}(t) + \boldsymbol{\gamma}(t) & \text{if } t_o \leq t \leq t_f - \epsilon_u \\ \mathbf{0}_{3 \times 1} & \text{otherwise} \end{cases} \quad (33)$$

where $\epsilon_u > 0$ can be selected to be arbitrary small.

3.1 Optimal Rendezvous Time

If the terminal time t_f is given, then $\mathbf{r}_s(t_f)$ and $\dot{\mathbf{r}}_s(t_f)$ can be computed from (22). However, the optimal terminal time, t_f^* remains to be found. The *optimal Hamiltonian* $\mathcal{H}^* = \mathcal{H}(\mathbf{x}^*, \mathbf{u}^*, \boldsymbol{\lambda})$ calculated at optimal point \mathbf{u}^* and \mathbf{x}^* must satisfy $\mathcal{H} = 0$, i.e.,

$$\mathcal{H}^*(t_f^*) = 1 - \kappa a^2 - 2\kappa \|\boldsymbol{\beta}\|^2 + \boldsymbol{\lambda}_s^T \dot{\mathbf{x}}_s = 0, \quad (34)$$

where $\mathbf{x}_s = [\mathbf{q}^T \ \boldsymbol{\omega}^T \ \mathbf{r}^T]^T$ is the state vector of the target. Equation (34) gives the extra equation required to determine the optimal terminal time. We will show in the following analysis that $\boldsymbol{\lambda}_s^T \dot{\mathbf{x}}_s$ can be expressed as a function of t_f . The final values of the costate can be obtained from the end point constraint equation referred to as the *transversality* condition:

$$\boldsymbol{\lambda}(t_f) = \left(\frac{\partial \psi}{\partial \mathbf{x}} \right)^T \boldsymbol{\nu} + \frac{\partial \phi}{\partial \mathbf{x}} \Big|_{\mathbf{x}(t_f)} \quad (35)$$

where vector $\boldsymbol{\nu} = [\boldsymbol{\nu}_1^T \ \boldsymbol{\nu}_2^T]^T$, where $\boldsymbol{\nu}_1, \boldsymbol{\nu}_2 \in \mathbb{R}^3$, is the Lagrangian multiplier owing to the constraint (21). Using (21) in (35) yields

$$\boldsymbol{\lambda}(t_f) = \begin{bmatrix} (\nabla_{\mathbf{x}_s} \mathbf{r}_s)^T \boldsymbol{\nu}_1 + (\nabla_{\mathbf{x}_s} \dot{\mathbf{r}}_s)^T \boldsymbol{\nu}_2 + \nabla_{\mathbf{x}_s} \phi \\ -\boldsymbol{\nu}_1 + \nabla_{\mathbf{r}_r} \phi \\ -\boldsymbol{\nu}_2 \end{bmatrix}_{\mathbf{x}(t_f)}. \quad (36)$$

Now, equating right-hand sides of (28) and (36) will result in a set of three equations with three unknowns $\boldsymbol{\nu}_1$, $\boldsymbol{\nu}_2$, and $\boldsymbol{\lambda}_s^T \dot{\mathbf{x}}_s$. Solving the set of equations gives the following useful identity

$$\boldsymbol{\lambda}_s^T \dot{\mathbf{x}}_s = (\nabla_{\mathbf{r}_r} \phi - 2\kappa \boldsymbol{\alpha})^T \dot{\mathbf{r}}_s + 2\kappa (\boldsymbol{\alpha}(t_f - t_o) + \boldsymbol{\beta})^T \dot{\mathbf{r}}_s + \nabla_{\mathbf{q}} \phi^T \dot{\mathbf{q}}, \quad (37)$$

Finally, substituting (37) into (34) and using the optimal motion trajectories, we will arrive at

$$\begin{aligned} \mathcal{H}(t_f) = & 1 - \kappa a^2 - 2\kappa \|\boldsymbol{\beta}\|^2 + 2\kappa \boldsymbol{\beta}^T \ddot{\mathbf{r}}_s + \frac{1}{2} \nabla_{\mathbf{q}} \phi^T \boldsymbol{\Omega}(\boldsymbol{\omega}) \mathbf{q} \\ & + (\boldsymbol{\beta}^T \nabla_{\mathbf{r}_r} \phi - 2\kappa \boldsymbol{\alpha}^T \boldsymbol{\beta} + 2\kappa \boldsymbol{\alpha}^T \ddot{\mathbf{r}}_s)(t_f - t_o) \\ & + \left(\frac{1}{2} \boldsymbol{\alpha}^T \nabla_{\mathbf{r}_r} \phi - \kappa \|\boldsymbol{\alpha}\|^2 \right) (t_f - t_o)^2 = 0 \end{aligned} \quad (38)$$

where the predicted acceleration, $\ddot{\mathbf{r}}_s(t_f)$ can be obtained from the time derivative of (22b) as

$$\ddot{\mathbf{r}}_s = \mathbf{A}(\mathbf{q}) \left(\boldsymbol{\omega} \times (\boldsymbol{\omega} \times \boldsymbol{\rho}) + \mathbf{d}(\boldsymbol{\omega}) \times \boldsymbol{\rho} \right).$$

The zero crossing solution, i.e., optimal rendezvous time, of the explicit equation (38) can be obtained using a numerical method such as the Newton-Raphson (NR) method.

4 Post-Grasping Trajectory Planning

After grasping the uncontrolled drifting and tumbling space object by the manipulator, the manipulator should gently exert force and torque to the object for stopping the drift. This section describes robot trajectory planning for dissipation of the angular and linear momentums of the grasped object in minimum time so that the magnitude of the interaction force and torque between the manipulator's end-effector and the tumbling satellite are upper-bounded. We assume that *a priori* estimates of target mass, m , and the trace of its inertia tensor are available. Therefore, the absolute inertia can be computed from the estimations of the relative inertia by

$$I_{xx} = \frac{\text{tr}(\mathbf{I}_c)}{b_x(\mathbf{p})}, \quad I_{yy} = \frac{\text{tr}(\mathbf{I}_c)}{b_y(\mathbf{p})}, \quad I_{zz} = \frac{\text{tr}(\mathbf{I}_c)}{b_z(\mathbf{p})}$$

Denoting the linear and angular momentums of the target as $\mathbf{h} = \mathbf{I}_c \boldsymbol{\omega}$ and $\mathbf{p} = m\mathbf{v}$, we can write the dynamics of the target in the post-grasping phase

$$\dot{\mathbf{p}} + \boldsymbol{\omega} \times \mathbf{p} = \mathbf{f} \quad (39a)$$

$$\dot{\mathbf{h}} + \boldsymbol{\omega} \times \mathbf{h} = \boldsymbol{\tau} - \boldsymbol{\rho} \times \mathbf{f}, \quad (39b)$$

where \mathbf{f} and $\boldsymbol{\tau}$ are the force and torque exerted by the robot's end-effector to the target. The objective is to damp out the initial linear and angular momentums of the target right after grasping, i.e., $\mathbf{p}(0)$ and $\mathbf{h}(0)$, as quickly as possible subject to the force and torque limits. That is, the torque and force trajectories should satisfy

$$\|\mathbf{p}\| \rightarrow 0 \quad \text{and} \quad \|\mathbf{h}\| \rightarrow 0$$

$$\text{s.t.} \quad \|\mathbf{f}\| \leq f_{\max} \quad (40)$$

$$\|\boldsymbol{\tau}\| \leq \tau_{\max} \quad (41)$$

Define positive function

$$V = \|\mathbf{p}\| + \|\mathbf{h}\| \quad (42)$$

Then, the time-derivative of V along trajectories of (39) yields

$$\begin{aligned} \dot{V} &= \frac{\mathbf{p}^T \dot{\mathbf{p}}}{\|\mathbf{p}\|} + \frac{\mathbf{h}^T \dot{\mathbf{h}}}{\|\mathbf{h}\|} \\ &= (\check{\mathbf{p}} - \boldsymbol{\rho} \times \check{\mathbf{h}})^T \mathbf{f} + \check{\mathbf{h}}^T \boldsymbol{\tau} \end{aligned} \quad (43)$$

where

$$\check{\mathbf{p}} = \frac{\mathbf{p}}{\|\mathbf{p}\|} \quad \text{and} \quad \check{\mathbf{h}} = \frac{\mathbf{h}}{\|\mathbf{h}\|} \quad (44)$$

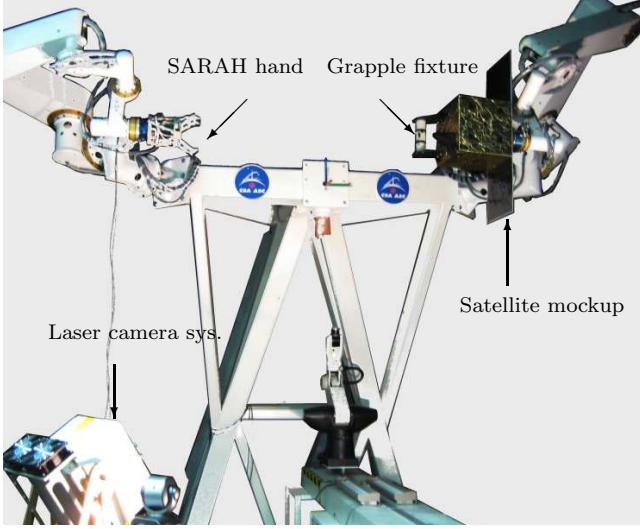


Figure 2: The experimental setup

are unit vectors in the directions of the linear and angular momentum vectors. It is clear from (43) that in order to dump the linear and angular momentums as quickly as possible given the force/moment limits (40), the force and torque should take the forms

$$\mathbf{f} = -\frac{\check{\mathbf{p}} - \boldsymbol{\rho} \times \check{\mathbf{h}}}{\|\check{\mathbf{p}} - \boldsymbol{\rho} \times \check{\mathbf{h}}\|} f_{\max} \quad (45a)$$

$$\boldsymbol{\tau} = -\check{\mathbf{h}} \tau_{\max} \quad (45b)$$

Finally, substituting (45) into (39), we arrive at the Cartesian motion trajectories

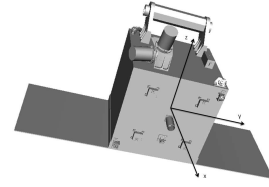
$$\dot{\boldsymbol{\omega}}^* = \mathbf{d}(\boldsymbol{\omega}) - \frac{\boldsymbol{\omega}}{\|\mathbf{I}_c \boldsymbol{\omega}\|} \tau_{\max}$$

$$\dot{\mathbf{v}}^* = -\boldsymbol{\omega} \times \mathbf{v} - \frac{\check{\mathbf{p}} - \boldsymbol{\rho} \times \check{\mathbf{h}}}{m \|\check{\mathbf{p}} - \boldsymbol{\rho} \times \check{\mathbf{h}}\|} f_{\max}$$

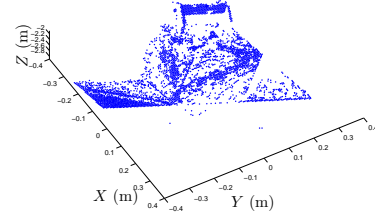
$$\ddot{\mathbf{r}}_r^* = \mathbf{A}(\mathbf{q})(\dot{\mathbf{v}}^* + \dot{\boldsymbol{\omega}}^* \times \boldsymbol{\rho} + \boldsymbol{\omega} \times (\boldsymbol{\omega} \times \boldsymbol{\rho}))$$

5 Experiment

This section reports experimental results showing the performance of the vision-guided robotic system for autonomous interception of a tumbling satellite. Fig. 2 illustrates the experimental setup with two manipulator arms. One arm is employed to drift and tumble the mockup of a target satellite according to dynamics motion in zero-gravity [13]. The other arm is used to autonomously approach the mockup and capture its grapple fixture. Neptec's Laser Camera System (LCS) [14] is used to obtain the range data at a rate of 2 Hz. The target pose is estimated by comparing the range data



(a) The satellite CAD model.



(b) The point-cloud data.

Figure 3: The ICP algorithm matches points from the CAD model and the scanned data to estimate the object pose.

obtained from the LCS against the CAD model of the mockup using the Iterative Closest Point (ICP) algorithm [15]. The ICP algorithm is an iterative procedure which minimizes a distance between point cloud in one dataset and the closest points in the other [16]. One dataset is a set of 3D point cloud acquired by scanning the target, while the other one is a CAD surface model as illustrated in Fig. 3.

The robotic arm to which the satellite mockup is attached is controlled so as to precisely mimic the dynamics motion of a target satellite. The moment of inertia values of the target satellite are selected as $I_{xx} = 4 \text{ kgm}^2$, $I_{yy} = 8 \text{ kgm}^2$, $I_{zz} = 5 \text{ kgm}^2$, and the location of CM is $\boldsymbol{\rho} = [-0.15 \ 0 \ 0]^T \text{ m}$. These values are used to determine the manipulator-driven motion of the target as free-floating object with initial drift velocity $\dot{\mathbf{r}}(0) = [-3 \ -2 \ 1.5] \text{ mm/s}$ and initial angular velocity $\boldsymbol{\omega}(0) = [0.09 \ -0.04 \ 0.03] \text{ rad/s}$.

The parameters of the optimal motion planner are set to $w_1 = 2$, $w_2 = 50$, $\kappa = 1000$, and $a = 0.01$. The time-history of the position and orientation of the mockup satellite obtained from ICP algorithm are shown in Fig. 4. Apparently, the vision system is obstructed by the robotic arm during its final approach at time $t = 112 \text{ s}$. and thereafter the visual pose measurements are incorrect. During the learning phase, the EKF estimator receives these noisy measurements and subsequently estimates the sets of inertial parameters plus the linear and angular velocities of the tumbling satellite. Figs. 5 and 6 show the trajectories of

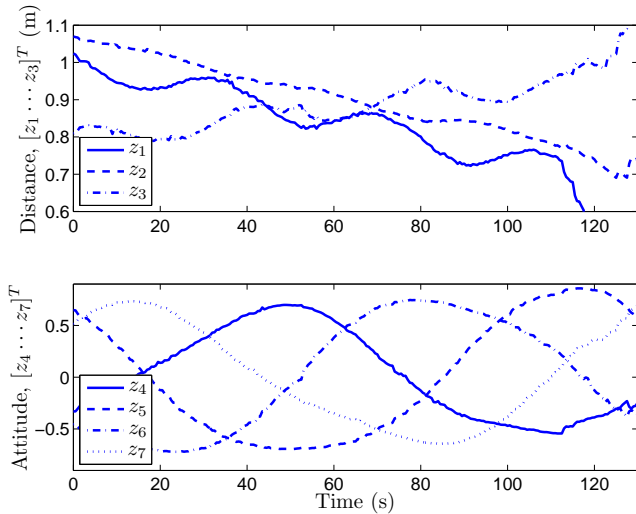


Figure 4: Target pose measurements obtained from LCS.

the estimated velocities and the inertial parameters, respectively. The motion planner automatically generates robot trajectory once the EKF estimator converges. To this end, the convergence is when the Euclidean norm of the state covariance matrix drops below a threshold ϵ_{th} , i.e., $\|\mathbf{P}_k\| \leq \epsilon_{th}$. The time-history of the norm of the covariance matrix is plotted in Fig. 7. In this experiment, the threshold value for the convergence detection is set to 0.1. Apparently, at time $t = 85$ s, the trajectory reaches the prescribed threshold $\epsilon_{th} = 0.1$ indicating the filter convergence. The initial time, however, is set to $t_o = 90$ s, leaving a margin of 5 s to accommodate the computation time needed for path planning. Trajectories of predicted position, velocity, and acceleration of the grapple fixture calculated from the latest estimation of the motion states and parameters of the target are shown in Fig. 8. A comparison of the trajectories of the visual measurements and those of the predicted position in Fig. 8a reveals that the visual measurements are not reliable at the final stages of the robot approach after time $t = 112$ s. The optimal rendezvous time, t_f , is obtained from solving the Hamiltonian as function of t_f in (38) using the predicted motion trajectories. The zero-crossing of the Hamiltonian numerically is found (using the Newton-Raphson method) to be

$$t_o = 90 \text{ s} \quad \text{and} \quad t_f = 126.5 \text{ s}$$

as illustrated in Fig. 9. Trajectories of the robot's end-effector and the satellite grapple fixture are shown in Fig. 10. It is evident that the robot intercepts the handle at the designated final time. Fig. 11(a) is a phase plane showing trajectories of the distance between the

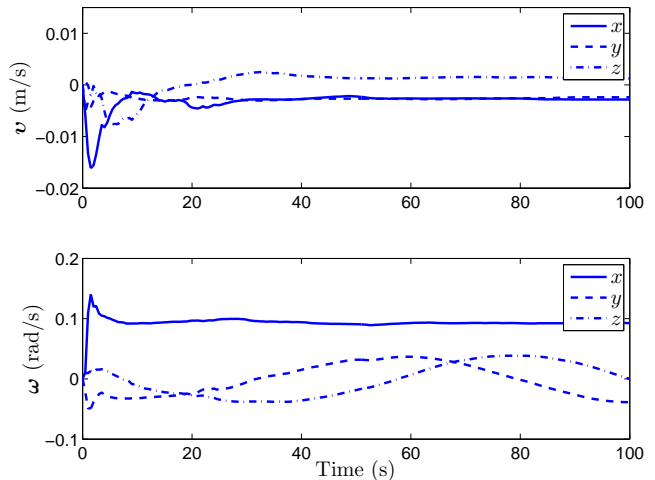


Figure 5: Estimated drift velocity and angular velocity of the target.

end-effector and the grapple fixture, $\mathbf{r}_s - \mathbf{r}_r$ versus the relative velocity, $\dot{\mathbf{r}}_s - \dot{\mathbf{r}}_r$. It is clear from the plot that the end-effector has reached the grapple fixture with almost zero relative velocity. The predicted trajectories of the line-of-sight angle in Fig. 11(b) shows that the robot reaches the target at angle $\theta = 21^\circ$, which is small angle for reliable capture.

6 Conclusion

Visual guidance of a robotic manipulator to first intercept and then stabilize a drifting and tumbling space object with uncertain dynamics has been presented. A Kalman filter was used to estimate the motion states and a set of dynamics parameters of the target based on noisy pose measurements of a laser camera system. The estimations of the states and parameters were used by the guidance scheme to optimally plan the trajectory of the robot's end-effector in the pre- and post-grasping phases. For the pre-grasping phase, an optimal trajectory was designed for intercepting a grapple fixture on the target minimizing a cost function as a weighted linear sum of travel time, distance, and cosine of a line-of-sight angle subject to acceleration limit. In the post-grasping phase, another optimal trajectory ensures that the drifting and tumbling object is brought to state of rest as quickly as possible subject to force and torque limits. Finally, experimental results illustrating the autonomous guidance of a robotic manipulator for the capture of a tumbling mockup satellite were reported.

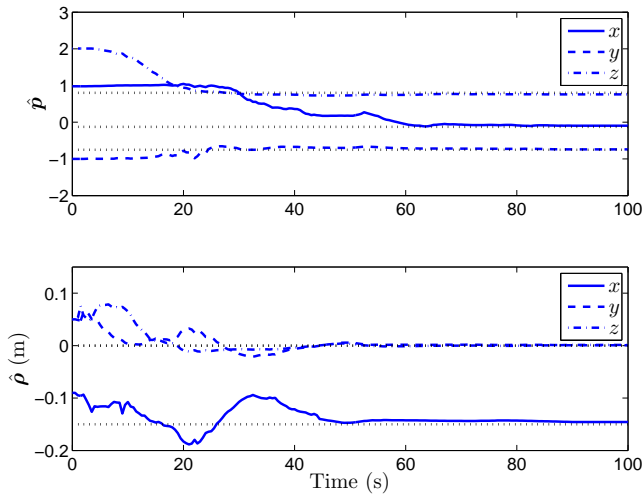


Figure 6: Convergence of the estimated dynamics parameters of the target to their true values (depicted by dotted-lines).

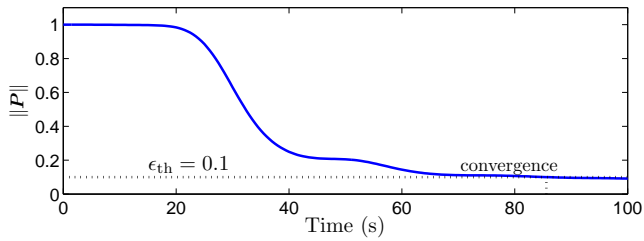


Figure 7: Detecting the estimator convergence from the norm of the state covariance matrix.

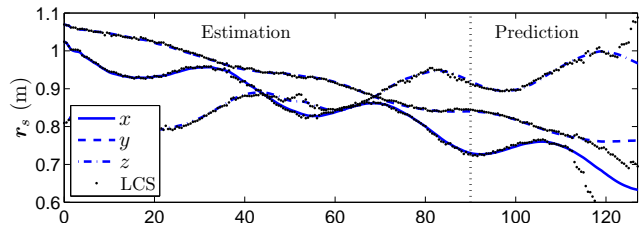


Figure 8: Estimations and predictions of the grapple-fixture position.

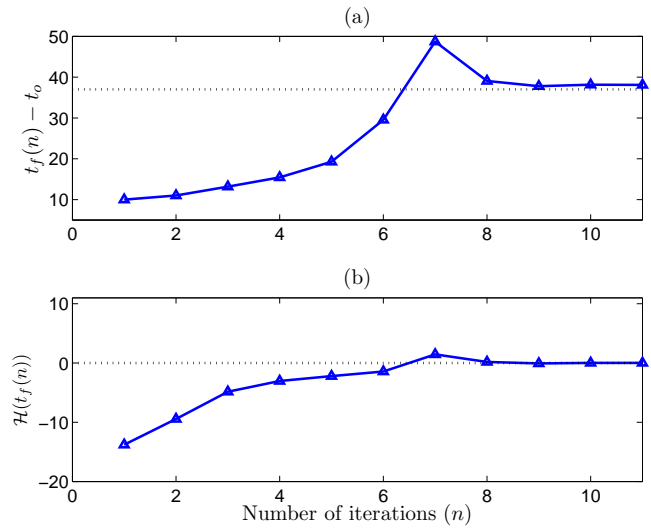


Figure 9: NR iterations to find the zero crossing of the Hamiltonian function.

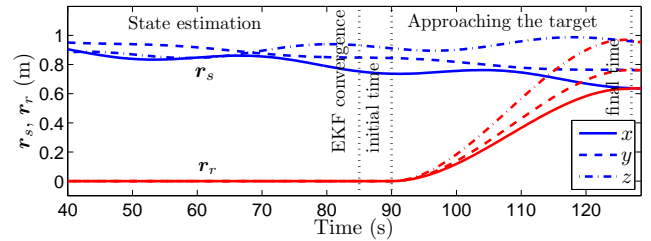


Figure 10: Position trajectories of the target satellite and the robot hand.

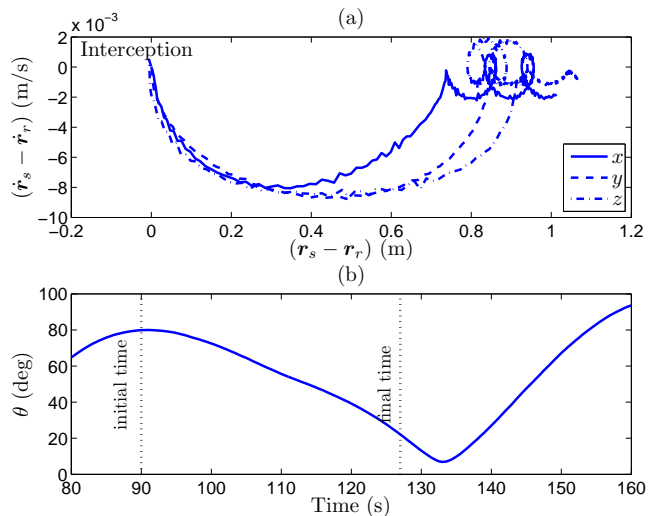


Figure 11: Trajectories of the relative position versus relative velocity (a); The line-of-sight angle (b).

References

- [1] G. Brachet, "Long-term sustainability of outer space activities," Committee on the Peaceful Uses of Outer Space (UNCOPUOS), Vienna, Tech. Rep., 8-19 February 2010.
- [2] D. Kessler, R. Reynold, and P. Ans-Meador, "TM 100-471 orbital debris environment for spacecraft designed to operate in low earth orbit," NASA JSC., Houston, TX, Tech. Rep., 1989.
- [3] J.-C. Liou, N. Johnson, and N. Hill, "Controlling the growth of future LEO debris populations with active debris removal," *Acta Astronautica*, vol. 66, no. 5-6, pp. 648–653, March-April 2009.
- [4] B. Barbee, S. Alfano, E. Pinon, K. Gold, and D. Gaylor, "Design of spacecraft missions to remove multiple orbital debris objects," in *Aerospace Conference, 2011 IEEE*, march 2011, pp. 1–14.
- [5] S. Kawamoto, S. Nishida, and S. Kibe, "Research on a space debris removal system," *NAL Res Prog (National Aerospace Lab. Japan)*, vol. 2002/2003, pp. 84–87, 2003.
- [6] D. Whelan, E. Adler, S. Wilson, and G. Roesler, "Darpa orbital express program: effecting a revolution in space-based systems," in *Small Payloads in Space*, vol. 136, Nov. 2000, pp. 48–56.
- [7] N. Inaba and M. Oda, "Autonomous satellite capture by a space robot: world first on-orbit experiment on a japanese robot satellite ets-vii," in *Robotics and Automation, 2000. Proceedings. ICRA '00. IEEE International Conference on*, 2000.
- [8] K. Yoshida, "Engineering test satellite VII flight experiment for space robot dynamics and control: Theories on laboratory test beds ten years ago, now in orbit," *The Int. Journal of Robotics Research*, vol. 22, no. 5, pp. 321–335, 2003.
- [9] G. Hirzinger, K. Landzettel, B. Brunner, M. Fisher, C. Preusche, D. Reintsema, A. Albuschaffer, G. Schreiber, and B.-M. Steinmetz, "DLR's robotics technologies for on-orbit servicing," *Advanced Robotics*, vol. 18, no. 2, pp. 139–174, 2004.
- [10] *On-Orbit Satellite Servicing Study, Project Report*, National Aeronautics and Space Administration, Goddard Space Flight Center, 2010.
- [11] F. Aghili, "A prediction and motion-planning scheme for visually guided robotic capturing of free-floating tumbling objects with uncertain dynamics," *IEEE Trans. on Robotics*, vol. 28, no. 3, pp. 634–649, June 2012.
- [12] B. D. O. Anderson and J. B. Moore, *Optimal Control*. Englewood Cliffs, NJ: Prince Hall, 1990.
- [13] F. Aghili and M. Namvar, "Scaling inertia properties of a manipulator payload for 0-g emulation of spacecraft," *The International Journal of Robotics Research*, vol. 28, no. 7, pp. 883–894, July 2009.
- [14] C. Samson, C. English, A. Deslauriers, I. Christie, F. Blais, and F. Ferrie, "Neptec 3D laser camera system: From space mission STS-105 to terrestrial applications," *Canadian Aeronautics and Space Journal*, vol. 50, no. 2, pp. 115–123, 2004.
- [15] F. Aghili, M. Kuryllo, G. Okouneva, and C. English, "Fault-tolerant position/attitude estimation of free-floating space objects using a laser range sensor," *IEEE Sensors Journal*, vol. 11, no. 1, pp. 176–185, Jan. 2011.
- [16] P. J. Besl and N. D. McKay, "A method for registration of 3-D shapes," *IEEE Trans. on Pattern Analysis & Machine Intelligence*, vol. 14, no. 2, pp. 239–256, 1992.